AIAA CFD 97-2099

Applications of the Space-Time Conservation Element/Solution Element Method to Unsteady Chemically Reacting Flows

Sheng-Tao Yu *
NYMA Technology, Inc.
NASA Lewis Research Center
Cleveland, OH

Sin-Chung Chang †
NASA Lewis Research Center
Cleveland, OH

Abstract

In this paper, we report the application of the CE/SE method to unsteady, chemically reacting flows. As a contrast to the modern upwind schemes, Riemannn solver and reconstruction procedure are not the building blocks of the present method. Therefore, the logic of the method is considerably simpler. Due to chemical reactions, stiff source terms exist in the species equations. The source terms are treated by a volumetric integration over space-time regions. The treatment results in a locally implicit formulation and Newton's method is used to solve the equation. We also assess the numerical resolution of the contact discontinuity between flow streams with different chemical species. Three examples are reported in the paper: (1) a planar shock wave passes a straight fast-slow gaseous interface, (2) a planar shock wave passes one and two circular fast-slow gaseous interfaces, and (3) supersonic combustion ignited by an oblique shock.

1 Introduction

Recently, Chang and coworkers [1-4] reported a new framework for the numerical solution of conservation laws, namely, the Method of Space-Time Conservation Element and Solution Element, or the CE/SE method for short. This method is distinguished by the simplicity of its conceptual basis, i.e., a unified treatment of flux conservation in space and time. The method was developed from fundamentals. It is not an incremental improvement of a previously existing method.

Essentially, the space-time domain, where the calculation is of interest, is divided into many Conservation Elements (CEs). In particular, the lattic stencil is based on a staggering spatial mesh, which zigzags as time evolves such that flow information at each interface separating adjacent CEs can be evaluated without using a Riemann solver. Inside each CE, the distribution of the flow solution is not calculated through a reconstruction procedure as that in the modern upwind schemes. Instead, the gradients of flow variables are treated as independent unknowns, and they are not influenced by the flow properties in neighboring elements at the same time level. This is in full compliance with the flow physics of the initial value problem. The resultant scheme is *explicit* in time and involves only *two time levels*. For flows in multiple spatial dimensions, *no directional splitting* is employed. The two and three-dimensional spatial meshes employed by the CE/SE method are built from triangles and tetrahedrons.

With the above construction of the CE/SE method, a family of schemes have been developed, namely, the a scheme for inviscid, isentropic flows, the $a - \mu$ for viscous flows, and the $a - \epsilon$ scheme for inviscid flows with shocks. Chang [2,3] showed that for inviscid and isentropic flows, the a scheme is neutrally stable

*Senior Engineer, styu@lerc.nasa.gov.
†Senior Scientist, vvscc@noboo.lerc.nasa.gov.

(non-dissipative) for CFL ≤ 1, and it can march forward and backward in time. For solving the Navier-Stokes equations, the $a - \mu$ scheme is unconditionally stable for various μ's, provided CFL ≤ 1. These features are important when solving viscous flows because the physical viscosity will not be overwhelmed by the numerical dissipation.

For flows with shocks, entropy increases across the shock. An artificial damping is added to the a scheme to satisfy the entropy increase condition, i.e., the $a - \epsilon$ scheme. This is necessary because the a scheme is neutrally stable, and does not allow any entropy increase. Within one marching step, the added artificial damping constrains the gradients of flow properties, while the flow properties themselves are calculated solely based on the space-time flux conservation. In particular, the $a - \epsilon$ scheme was designed such that no *priori* knowledge of the flow distribution, such as monotonicity and Total Variation Diminishing (TVD), is required. As a result, this formulation can be straightforwardly applied to solve conservation laws with source terms. Note that the flow solution is no longer monotonic (or TVD) when there is source term. In [5], we have reported the extension of the $a - \epsilon$ for solving conservation laws with stiff source terms in one spatial dimension.

In this paper, the treatment for stiff source terms is extended to solve equations in two spatial dimensions. Due to the merit of the CE/SE method, this extension is straightforward and we shall only illustrate its basic principle. In addition, we include several benchmark tests of shock induced mixing without chemical reaction. The purpose is to assess the the numerical resolution of the contact discontinuity between flow streams with different chemical species.

The rest of the paper is organized as follows. In Section 2, we discuss the space-time integration based on the conventional finite volume method as well as the CE/SE method. The roles of the source term in these two different approaches are clarified. In Section 3, we briefly discuss the space-time discretization of the conservation laws with stiff source terms in one and two spatial dimensions. In Section 4, we present the numerical examples. We then provide the concluding remarks.

2 Space-Time Integration

2.1 The Finite-Volume Method

Conventionally, the space-time flux balance of conservation laws is described by formulations in both Lagrangian and Eulerian frames. These two formulations can be bridged by Reynold's transport theorem:

$$\frac{d}{dt}\int_{V_t} u dV_t = \int_{V_t} \frac{\partial u}{\partial t} dV_t + \int_{S(V_t)} u\vec{v}\cdot d\vec{s}, \quad (2.1)$$

where u is the density of a conserved property, V_t denotes the spatial volume of integration at time t, $S(V_t)$ is the surface of V_t, and $d\vec{s} = d\sigma\,\vec{n}$ with $d\sigma$ and $\vec{n}$, respectively, being the area and the outward unit normal vector of a surface element on $S(V_t)$. The points inside V_t move with velocity $\vec{v}$, generating the motion of the volume. The left hand side of Eq. (2.1) is based on the Lagrangian frame, and the right hand side is based on the Eulerian frame. Note that space and time are treated in different manners.

Consider a scalar convection equation with a source term p,

$$u_t + \vec{\nabla}\cdot\vec{f} = p, \quad (2.2)$$

where $\vec{f} = u\vec{v}$ with $\vec{v}$ being the convection velocity. The integral counterpart to Eq. (2.2) is

$$\begin{aligned} &\frac{d}{dt}\int_{V_t} u dV_t, \\ &= \int_{V_t} \frac{\partial u}{\partial t} dV_t + \int_{S(V_t)} \vec{f}\cdot d\vec{s}, \\ &= \int_{V_t} p dV_t. \end{aligned} \quad (2.3)$$

To solve Eq. (2.3), the conventional finite-volume methods reformulate the equation based on *a fixed spatial domain*, i.e.,

$$\frac{\partial}{\partial t}\int_V u dV = -\int_{S(V)} \vec{f}\cdot d\vec{s} + \int_V p dV. \quad (2.4)$$

Alternatively, one could integrate Eq. (2.4) in time from t_1 to t_2, i.e.,

$$\int_V udV\Big|_{t_1}^{t_2} = \int_{t_1}^{t_2} dt \left(-\int_{S(V)} \vec{f} \cdot d\vec{s} + \int_V pdV \right). \tag{2.5}$$

Equation (2.5) depicts a clearer picture of the space-time flux balance as compared to Eq. (2.4).

As shown in Fig. 2.1(a), due to *the fixed spatial domain*, the shape of the space-time CEs in one spatial dimension must be rectangular. These elements must stack up exactly on top of each other in the time-direction, i.e., no staggering of CEs in time is allowed. In two spatial dimensions, as shown in Fig. 2.1(b), a conservation element is a uniform-cross-section cylinder in space-time, and again no staggering in time is allowed.

This arrangement results in vertical interfaces extended in the direction of time evolution between adjacent CEs. Across these interfaces, flow information travels in both directions. Therefore, upwind bias (or a Riemann solver) becomes necessary in calculating the interfacial flux.

2.2 Treatments of Stiff Source Terms

In calculating Eq. (2.5), we need to integrate the spatial fluxes $\vec{f}$ at the cell boundaries between two time steps. Usually, this calculation is approximated by a Riemann solver. The existence of the source term, however, will influence the Riemann solution at cell boundaries. Therefore, Roe and Arora [6] developed a dispersive Riemann solution following the characteristics, which are attenuated by the source term. Unfortunately, this method cannot be extended to multiple spatial dimensions. Note that directional splitting is commonly used in modern upwind scheme because there is no known analytical Riemann solution in multiple spatial dimensions. Source terms, however, have no direction, and cannot be split accordingly.

Alternatively, finite-differencing the time marching term in Eq. (2.4) can be adopted. This approach assumed a smooth temporal evolution of the flow properties. Applying this method to flows with propagating discontinuities cannot be justified. Here, the finite-volume methods concentrated on calculating the right hand side of Eq. (2.4). As such, the rate of change of u contained in V is equal to the combination of (i) the flux $\vec{f}$ across $S(V)$, and (ii) the integration of the source term over V. As such, fractional-step (or splitting) methods resort to strong measures of segregating the two effects and treating them in a sequential fashion. Colella et al. [7] and LeVeque and Yee [8] tried various fractional step methods. Reasonable results were obtained for non-stiff source terms. For stiff source terms, transient flow solutions bifurcated or moved in wrong speeds.

Perhaps, the most interesting approach in recent years is based on shooting for the equilibrium state of the relaxation system [9]. In this setting, Jin [10] incorporated the physical asymptotics of the relaxation system into the numerical scheme using a Runge-Kutta method coupled with a stiff ODE solver. Successful results were obtained for flow equations with stiff source terms. The method, however, requires some knowledge of the asymptotics of the relaxation system. In addition, the application of the asymptotics is based on the assumption that the flow field is smooth.

2.3 The Space-Time Integration of the CE/SE Method

In the CE/SE method, space and time are treated in a unified manner. Consider a set of M coupled convection equations in one spatial dimension:

$$\mathbf{U}_t + \mathbf{F}_x = \mathbf{P}, \quad \mathbf{U} \in \mathbf{R}^M, \tag{2.6}$$

where $\mathbf{U}$ is the unknown vector, $\mathbf{F}$ is the spatial flux vector, and $\mathbf{P}$ is the source term vector. As shown in Fig. 2.2, let $x_1 = x$, and $x_2 = t$ be the coordinates of a two-dimensional Euclidean space E_2, and all mathematical operations, such as div, curl, and grad, can be carried out as if E_2 was an ordinary two-dimensional Euclidean space. Thus, Eq. (2.6) can be expressed as M

scalar equations:

$$\nabla \cdot \vec{\mathbf{h}}_m = p_m \quad m = 1, 2, \ldots, M \tag{2.7}$$

where $\vec{\mathbf{h}}_m = (f_m, u_m)$, and f_m, u_m, and p_m are the mth components of $\mathbf{F}$, $\mathbf{U}$, and $\mathbf{P}$, respectively. Equation (2.7) is valid everywhere in E_2 for continuous flow solutions. For solutions with discontinuities, an integral counterpart to Eq. (2.7) must be employed:

$$\oint_{S(R)} \vec{\mathbf{h}}_m \cdot d\vec{s} = \int_R p_m dR, \quad m = 1, 2, \ldots, M \tag{2.8}$$

where $S(R)$ is the boundary of a space-time region R, and $d\vec{s}$ represents a surface element of $S(R)$. Equation (2.8) is obtained by using Gauss' divergence theorem.

Equation (2.8) states that the total space-time flux of $\vec{\mathbf{h}}_m$ leaving R through its boundary is equal to the integration of the source term p_m over the space-time region R. As a contrast to the finite-volume method, Eqs. (2.4-5), the present formulation does not impose any constraint on the shape of the CEs in the space-time domain. This is the crucial difference that, at the conceptual level, separates the CE/SE method from the finite-volume method.

We remark that the conventional space-time integration Eq. (2.5) is a special case of Eq. (2.8). For flows in one spatial dimension using *a fixed spatial domain* for CEs, the left hand side of Eq. (2.8) can be converted into a line integration, i.e.,

$$\oint_{S(R)} \vec{\mathbf{h}}_m \cdot d\vec{s} = \oint_{S(R)}^{c.c.} (f_m dt - u_m dx), \quad m = 1, 2, \ldots, M \tag{2.9}$$

where *c.c.* indicates that the line integration is carried out in the counterclockwise direction. Obviously, Eq. (2.8) is equivalent to Eq. (2.5) under this condition.

3 The Space-Time Discretization

3.1 One Spatial Dimension

Based on Eq. (2.8), we are ready to construct the space-time discretization for conservation laws with source terms. In Fig. 3.1, we show the nodal locations where the unknowns are stored. The space and time intervals between neighboring nodes are denoted by $\Delta x/2$ and $\Delta t/2$. The Solution Element (SE) associated with each node (j, n) is rhombic. Refer to Fig. 3.2. Inside a SE, the flow properties are assumed continuous, and is discretized by a first-order Taylor expansion of x and t with respect to the mesh node (x_j, t^n). Between SEs, discontinuities are allowed. The union of all SEs covers the whole space-time domain. The CEs, on the other hand, are space-time regions, over which the space-time flux balance will be enforced. In general, a CE could coincide with a SE, or take other shape. The flow solution inside a CE does not have to be smooth.

First, we specify a CE that coincides with the SE(j, n) and impose the space-time flux balance over the rhombic region,

$$\oint_{S(\mathrm{CE}(j,n))} \vec{\mathbf{h}}^*_m \cdot d\vec{s} = \int_{\mathrm{CE}(j,n)} p^*_m dR, \quad m = 1, 2, \ldots, M, \tag{3.1}$$

where $\vec{\mathbf{h}}^*_m$ is the discretized space-time flux vector. Refer to Eqs. (2.7-8). Apply Gauss' divergence theorem, and we get

$$\int_{\mathrm{CE}(j,n)} \left[(f_{m,x})^n_j + (u_{m,t})^n_j - p^*_m \right] dR = 0. \tag{3.2}$$

Let

$$\bar{p^*_m}{}^n_j = \int_{\mathrm{CE}(j,n)} p^*_m dR / \diamond, \tag{3.3}$$

with

$$\diamond = \int_{\mathrm{CE}(j,n)} dR \tag{3.4}$$

being the space-time volume of CE(j, n). As a result, Eq. (3.2) can be written as

$$\left[(f_{m,x})^n_j + (u_{m,t})^n_j - (\bar{p^*_m})^n_j \right] \diamond = 0, \tag{3.5}$$

or

$$(f_{m,x})_j^n + (u_{m,t})_j^n - (p_m^*)_j^n = 0. \qquad (3.6)$$

With the aid of Eq. (3.6), $(u_{m,t})_j^n$ can be determined in terms of $(u_m)_j^n$ and $(f_{m,x})_j^n$, for $m = 1, 2, \ldots, M$. Therefore, the distributions of flow properties inside SE(j,n) are determined by $\mathbf{U}_j^n$, and $(\mathbf{U}_x)_j^n$. Note that $\mathbf{U}_j^n$, and $(\mathbf{U}_x)_j^n$ are the independent variables to be calculated in the CE/SE method.

Next, as shown in Fig. 3.3, we impose space-time flux conservation over two square CEs, denoted by CE$_-(j,n)$ and CE$_+(j,n)$, i.e.,

$$\oint_{S(CE_-)} \vec{\mathbf{h}}_m^* \cdot d\vec{s} = \overset{\diamond}{\frac{}{4}} \left((p_m)_{j-1/2}^{n-1/2} + (p_m)_j^n \right), \qquad (3.7)$$

$$\oint_{S(CE_+)} \vec{\mathbf{h}}_m^* \cdot d\vec{s} = \overset{\diamond}{\frac{}{4}} \left((p_m)_{j+1/2}^{n-1/2} + (p_m)_j^n \right). \qquad (3.8)$$

Note that CE$_-(j,n)$ is the union of $\triangle A'C'B'$ and $\triangle ABC$, and CE$_+(j,n)$ is the union of $\triangle A"D"C"$ and $\triangle ACD$.

Equation (3.7) leads to M relations involving the independent unknowns $\mathbf{U}_j^n$, $(\mathbf{U}_x)_j^n$, $\mathbf{U}_{j-1/2}^{n-1/2}$, and $(\mathbf{U}_x)_{j-1/2}^{n-1/2}$, and Eq. (3.8) leads to the other M relations involving $\mathbf{U}_j^n$, $(\mathbf{U}_x)_j^n$, $\mathbf{U}_{j+1/2}^{n-1/2}$, and $(\mathbf{U}_x)_{j+1/2}^{n-1/2}$. Since $\mathbf{U}_{j-1/2}^{n-1/2}$, $(\mathbf{U}_x)_{j-1/2}^{n-1/2}$, $\mathbf{U}_{j+1/2}^{n-1/2}$, and $(\mathbf{U}_x)_{j+1/2}^{n-1/2}$ are known, the $2M$ components of $\mathbf{U}_j^n$ and $(\mathbf{U}_x)_j^n$ are determined by Eqs. (3.7-8). Furthermore, $(p_m)_j^n$ in Eqs. (3.7-8) is a function of $(u_m)_j^n$. Therefore, Eqs. (3.7-8) are implicit equations of $\mathbf{U}_j^n$ and $(\mathbf{U}_x)_j^n$. To solve them, Newton's method is used. Usually, two or three Newton's steps are needed for a satisfactory convergence.

Unfortunately, when the source terms are stiff, the above method fails. Essentially, small differences between $(u_m)_{j-1/2}^{n-1/2}$ and $(u_m)_{j+1/2}^{n-1/2}$ will be amplified and result in huge differences between $(p_m)_{j-1/2}^{n-1/2}$ and $(p_m)_{j+1/2}^{n-1/2}$. That difference will in turn causes big difference between $(u_{m,t})_{j-1/2}^{n-1/2}$ and $(u_{m,t})_{j+1/2}^{n-1/2}$. Refer to Eq. (3.6). As a result, the numerical calculation for $(u_m)_j^n$ and $(u_{m,x})_j^n$ by Eqs. (3.7-8) is contaminated by the round-off errors, and the iterative procedure in Newton's method fails to converge.

The remedy is to avoid the amplification effect by re-distributing the space-time region of SE such that all source-term effects hinge on the mesh node (x_j, t^n) at the new time level. As shown in Fig. 3.4, the new SEs take the shape of a rectangular area with a line segment sticking out on the top of the rectangle. In this new construction, we impose the space-time flux balance over the same CE$_-$ and CE$_+$. However, the calculation is different in the following two aspects: (i) the calculation of $(u_{m,t})_{j\pm1/2}^{n-1/2}$ is simply by using

$$(u_{m,t})_{j\pm1/2}^{n-1/2} + (f_{m,x})_{j\pm1/2}^{n-1/2} = 0. \qquad (3.9)$$

Here, no source term effect is included. In the nomenclature of computational reactive flows, a frozen model is used. (ii) the integration of the source term over the space-time regions is calculated totally based on the flow properties at (x_j, t^n), i.e.,

$$\oint_{S(CE_-)} \vec{\mathbf{h}}_m^* \cdot d\vec{s} = \frac{\Delta x \Delta t}{2} (p_m)_j^n, \qquad (3.10)$$

$$\oint_{S(CE_+)} \vec{\mathbf{h}}_m^* \cdot d\vec{s} = \frac{\Delta x \Delta t}{2} (p_m)_j^n. \qquad (3.11)$$

Similar to that in the previous construction, we have $2M$ equations for $2M$ unknowns, and flow solution at the new time step can be determined.

3.2 Two Spatial Dimensions

The space-time discretization of Eq. (2.8) based on the CE/SE method in two spatial dimensions is a direct extension of that in one spatial dimension. Details of the CE/SE method for conservation laws without source term in two spatial dimensions are available in [2].

For conservation laws in two spatial dimensions, three unknowns are to be determined at each mesh point for each conservation equation:

u, u_x, u_y, where u is the density of a conserved property. Therefore, three sets of space-time conservation conditions are required at each mesh point. Figure 3.5 shows a two-dimensional spatial domain formed by congruent triangles with each triangle marked by either a filled or an open circle. The filled and the open circles represent mesh points at two consecutive time steps.

The three-dimensional SE in space-time domain takes a screw-driver shape as shown in Fig. 3.6. Within the SE, flow properties are smooth and are discretized by the first-order Taylor's series expansion. Across SEs, discontinuity of flow property is allowed. First, we impose the space-time flux balance over SE(i,j,n), where flow properties and their gradients at mesh point (x_i, y_j, t_n) are te be determined.

$$\oint_{S(\mathrm{CE}(i,j,n))} \vec{\mathbf{h}}_m^* \cdot d\vec{s} = \int_{\mathrm{CE}(i,j,n)} p_m^* dR, \quad m = 1,2,\ldots,M, \tag{3.12}$$

where $\vec{\mathbf{h}}_m^* = ((f_m^x)^*, (f_m^y)^*, u_m^*)$ is the discretized space-time flux vector. Apply Gauss' divergence theorem to Eq. (3.12), and we get

$$\int_{\mathrm{CE}(i,j,n)} \left[(f_{m,x}^x)_{i,j}^n + (f_{m,y}^y)_{i,j}^n + (u_{m,t})_{i,j}^n - p_m^*\right] dR = 0. \tag{3.13}$$

Let

$$\bar{p_m^*}{}_{i,j}^{n} = \int_{\mathrm{SE}(i,j,n)} p_m^* dR/\mathbf{V}, \tag{3.14}$$

with

$$\mathbf{V} = \int_{\mathrm{CE}(j,n)} dR \tag{3.15}$$

being the space-time volume of SE(i,j,n). As a result, Eq. (3.13) can be written as

$$(f_{m,x}^x)_{i,j}^n + (f_{m,y}^y)_{i,j}^n + (u_{m,t})_{i,j}^n - (\bar{p_m^*})_{i,j}^n = 0. \tag{3.16}$$

Using Eq. (3.16), $(u_{m,t})_{i,j}^n$ can be determined in terms of $(u_m)_{i,j}^n$, $(f_{m,x}^x)_{i,j}^n$, and $(f_{m,y}^y)_{i,j}^n$, for $m = 1,2,\ldots,M$. Therefore, the distributions of flow properties inside SE(i,j,n) are determined.

Recall the the amplification effect caused by the stiff source term as discussed in the last section. When the source term is stiff, small differences between the flow properties in the three neighboring nodes will be amplified and cause huge differences between source terms $\bar{p}_m^*$ in the three neighboring nodes. According to Eq. (3.16), this results in huge differences of u_{mt}^* between the three neighboring nodes. Consequently, the discretized space-time flux conservation will be contaminated by the round-off errors.

The remedy is to avoid the amplification effect by re-distributing the space-time regions such that all source-term effects hinge on the mesh node at the new time level. As shown in Fig. 3.7, the new SEs take the shape of a hexagonal cylinder with three surfaces sticking out on the top of the cylinder. As such, the calculation of u_{mt} in each SE is simply by

$$u_{m,t}^* + (f_{m,x}^x)^* + (f_{m,y}^y)^* = 0. \tag{3.17}$$

Here, no source-term effect is included, i.e., a frozen model is used.

We then impose three space-time flux balance conditions over three CEs as shown in Fig. 3.8. Each CE takes the shape of a parallelepiped. Here, the integration of the source term over the space-time regions is calculated totally based on the flow properties at the new time step. Here, we take the node (x_i, y_j, t^n) at the new time step, where unknowns are to be solved.

$$\oint_{S(CE_1)} \vec{\mathbf{h}}_m^* \cdot d\vec{s} = \frac{\mathbf{V}}{3}(p_m)_{i,j}^n, \tag{3.18}$$

$$\oint_{S(CE_2)} \vec{\mathbf{h}}_m^* \cdot d\vec{s} = \frac{\mathbf{V}}{3}(p_m)_{i,j}^n, \tag{3.19}$$

$$\oint_{S(CE_3)} \vec{\mathbf{h}}_m^* \cdot d\vec{s} = \frac{\mathbf{V}}{3}(p_m)_{i,j}^n. \tag{3.20}$$

Equations (3.18-20) are $3M$ correlations for $3M$ unknowns, and flow properties and their gradients at (x_i, y_j, t^n) can be determined. In addition, $(p_m)_{i,j}^n$ in Eqs. (3.18-20) is a function of $(u_m)_{i,j}^n$. As a result, Eqs. (3.18-20) are implicit relations of $(u_m)_j^n$, $(u_{mx})_j^n$, and $(u_{my})_j^n$. Newton's method is used to solve the equation set.

4 Numerical Examples

4.1 A Planar Shock Wave Passes A Straight Gaseous Interface

When a planar shock wave crosses a gaseous interface of different species, shock-wave refraction, reflection, and transmission take place. The complex interaction between the shock wave and the gaseous interface usually causes significant roll-up of the gaseous interface. This flow phenomenon was identified as a favorable mechanism to enhance mixing in supersonic combustion. The flow phenomenon was illustrated as shock induced Rayleigh-Taylor instability or the Richtmyer-Meshkov instability. The theory of wave impedance was also employed to study the flow physics. More recently, Picone and Boris [11] showed that misalignment of the pressure and density gradients leads to a source of vorticity:

$$\frac{d\omega}{dt} + \omega \nabla \cdot \mathbf{v} = \omega \cdot \nabla \mathbf{v} + \frac{\nabla\rho \times \nabla p}{\rho^2}. \qquad (4.1)$$

In this paper, we apply the CE/SE method to simulate this complex flow phenomenon. When solving the flow equations of two different species, a species equation is added to the Euler equations. The transportation of the other species can be determined by the mass conservation equation. In this case, the perfect gas law is used, and pressure is given by

$$p = (\gamma - 1)\left[\rho e - \frac{\rho}{2}(u^2 + v^2)\right], \qquad (4.2)$$

where the specific heat ratio of the gas mixture

$$\gamma = \frac{\frac{\gamma_1\rho_1}{M_1(\gamma_1-1)} + \frac{\gamma_2\rho_2}{M_2(\gamma_2-1)}}{\frac{\rho_1}{M_1(\gamma_1-1)} + \frac{\rho_2}{M_2(\gamma_2-1)}}, \qquad (4.3)$$

where M_i is the molecular weight for species i. The flow conditions are taken from the experimental and computational results reported by Zeng and Takayama [12]. An air/He interface is considered. The molecular weight of He is lighter than that of air. For the same temperature, the speed of sound inside He is faster. Therefore, air is the slow gas and He is the fast gas. In our calculations, the mesh size is 180×120.

Figure 4.1 shows density contours of the flow fields with three different angles of gaseous interfaces: 44^o, 58^o, and 77^o. The incident shock moves from left to right with Mach number equal to 1.4. When the shock hits the gaseous interface, a reflected shock and a transmitted shock are form. Across the interface, the primary shock is refracted. The reflected shock propagates to the left of the interface in a circular fashion, and the transmitted shock propagates to the right of the interface. When the incident angle α is less than a critical value, three shocks intersect one another at one point on the interface. When α is larger than the critical value, the transmitted shock tends to run away from the intersection point, and a free precursive wave shows up in front of the incident shock. For a shock with Mach number 1.4 interacting an air/He interface, the critical α is approximately 25^o.

Another special feature of the flow field is the crater near the bottom surface. At the muzzle of the crater, pressure drops and flow is accelerated as if there is an air jet charging into He. As a result, a vortex ring is form and tremendous mixing occurs between air and He. The results compared well with the experimental and CFD results reported in [12].

4.2 Planar Shock Wave Passes Circular Gaseous Interface

The last numerical example is extended to a planar shock interacting with circular Air/He interfaces. The basic features of this flow field are similar to that in the last numerical example. As reported by Yang et al. [13], this two-dimensional unsteady flow is an analogy to the three-dimensional steady flow produced by an oblique shock impinging on a light gas jet. The light gas jet is immersed in a coflowing, supersonic air stream. This flow mechanism can greatly enhance the mixing of the light and heavy gases. Essentially, the generated vorticity can stretch the gaseous interface such that the den-

sity and species gradients across the interface are intensified. As a result, the diffusive effect becomes important.

Figure 4.2 shows the density contours of the evolving flow fields. The Mach number of the incident shock is 1.2. The mesh size is 480×120. Initially ($t < 0.25$), the angle between the incident shock and the gaseous interface is very small, and the incident shock, the reflected shock, and the transmitted shock intersect one another on the interface. Since the interface is circular, the incident angle increases as time evolves. When $t > 0.4$, the flow becomes supercritical, i.e., the transmitted shock runs away to the right and a precursive wave is created. Note that full computational domain is plotted in Fig. 4.3. During $2.01 < t < 2.55$, the normal shock propagates smoothly out of the computational domain.

Figure 4.3 shows the temporal evolution of two He bubbles interacting with a planar shock. Initially, two identical bubbles are placed one radius apart. During $1.78 < t < 3.28$, the transmitted shocks and the precursive waves interact with one another and creats a weaker precursive wave ($t = 1.78$), which, later on, is caught up by the primary incident shock ($2.78 < t < 3.28$). At the later stage of the vortex roll-up, due to the low-pressure region behind the bubble, the left He bubble is sucked into the muzzle of the other highly stretched bubble.

4.3 Shock Ignited Combustion

In this case, we consider the combustion of a supersonic premixed H_2-air flow in a ramped duct. Similar calculations were reported in several previous works [15,16,17]. In the present calculations, we adopt a global finite-rate chemistry model for H_2-air reaction, originally developed by Taki and Fujiwara [14].

Two inlet temperatures are considered: 900 K and 1200 K, which are below the ignition threshold. The pressure of the free stream is about 1 atm, and the Mach number is 4. The mixture ratio of the H_2/air is stochiometric. The angle of the ramp is 10^o. Figure 4.4 shows the flow solution of the 900 K case. The higher temperature and pressure behind the ramp shock ignite the premixed gas. Behind the shock, the heat release due to the chemical reaction results in a continual pressure increase, which in turn causes the ramp shock to bend upward. Note that in all previous calculations, the shape of the upward-bending ramp shock was a smooth curve. In our calculations, however, we observe a distinct change of the shock angle. In addition, we observe fine ripples travel back and forth along the detonation front. Similar instability was reported in [15,16]. However, previous calculations were too diffusive to resolve the waves.

Figure 4.5 shows the comparison of pressure and temperature between the present calculations and the previous results. The distributions of T and P are obtained from $y = 0.13$ cm above the bottom wall. Three earlier tests with different numerical schemes were considered, including an LU [15], a PNS [16], and a TVD [17] schemes. Although different chemical models were used in these calculations, the comparison was reasonable.

5 Concluding Remarks

In this paper, we apply the CE/SE method to solve chemical reacting flows. By an unified treatment of space and time, source terms are included as a volumetric integral over space-time conservation elements. Moreover, for stiff source terms, the amplification effect must be eliminated. And a re-distribution of the space-time region was adopted such that the source-term effects hinge solely on the mesh nodes at new time level. As a result, the method is robust and stable for solving the conservation laws with underresolved stiff source terms. This new method is used to solve shock ignited combustion , and the results compare favorably with previously published data. In addition, in order to assess the numerical resolution of the contact discontinuity of different species, numerical tests of a planar shock wave passes gaseous interfaces were con-

ducted. The results compared well with previous experimental and computational results.

6 Acknowledgments

The first author wants to thank Dr. Robert Stubbs of NASA Lewis Research Center for the financial support of this research project.

References

[1] S.C. Chang and W.M. To, "A New Numerical Framework for Solving Conservation Laws – The Method of Space-Time Conservation Element and Solution Element," NASA TM 104495, August 1991.

[2] S.C. Chang, X.Y. Wang and C.Y. Chow, "New Developments in the Method of Space-Time Conservation Element and Solution Element – Applications to Two-Dimensional Time-Marching Problems", NASA TM 106758, December 1994.

[3] S.C. Chang, *J. Comput. Phys.*, **119**, (1995) pp. 295-324.

[4] S.C. Chang, S.T. Yu, A. Himansu, X.Y. Wang, and C.Y. Loh, "The Method of Space-Time Conservation Element and Solution Element – A New Paradigm for Numerical Solution of Conservation Laws," to appear in *Computational Fluid Dynamics Review 1996*, Edited by M.M. Hafez and K. Oshima, John Wiley and Sons, West Sussex, UK.

[5] S.T. Yu and S.C. Chang, "Treatments of Stif Source Terms in Conservation Laws by the Method of Space-Time Conservation Element and Solution Element," AIAA Paper 97-0435, January 1997.

[6] P.L. Roe and M. Arora, *Numer. Methods for Partial Diff. Equations*, **9** (1993) pp.459-505.

[7] P. Colella, A. Majda, and V. Roytburd, *SIAM J. Sci. Stat. Comput.*, **7**, 4 (1986) pp. 1059-1080.

[8] R.J. LeVeque and H.C. Yee, *J. Comput. Phys.*, **86** (1990) pp. 187-210.

[9] R.B. Pember, *SIAM J. Appl. Math.*, **53**, 5 (1993) pp. 1293-1330.

[10] S. Jin, *J. Comput. Phys.*, **122** (1995) pp. 51-67.

[11] J.M. Picone and J.P. Boris, *J. Fluid Mech.*, **189** (1988) pp. 23-51.

[12] S. Zeng and K. Takayama, *Acta Astronautica*, **38**, No. 11 (1966) pp.829-838.

[13] J. Yang, T. Kubota, and E.E. Zukoski, *AIAA J.*, **31** (1993) pp. 854-862.

[14] S. Taki and T. Fujiwara, *AIAA J.*, **16** (1978) pp. 73-77.

[15] S. Shuen and S. Yoon, *AIAA J.*, **27** (1989) pp 1752-1760.

[16] T. Chitsomboon, A. Kumar, and S.N. Tiwari, "Numerical Study of Finite-Rate Supersonic Combustion Using Parabolized Euqations," AIAA Paper 87-0088, January 1987.

[17] J.L. Shinn, H.C. Yee, and K. Uenishi, "Extension of a Semi-Implicit Shock Capturing Scheme for Three-Dimensional Fully Coupled Chemically Reactive Flows in Generalized Coordinate Systems," AIAA Paper 87-1577, 1987.

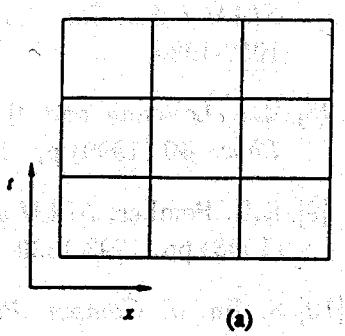

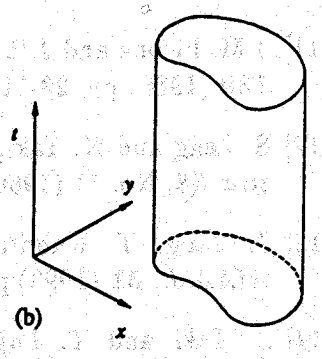

Fig. 2.1 Space-time conservation elements for methods using a fixed spatial domain: (a) one spatial dimension, and (b) two spatial dimensions.

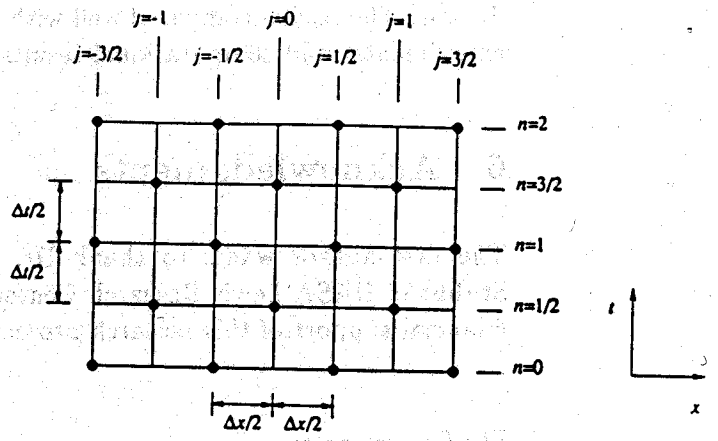

Fig. 3.1 The space-time mesh of the CE/SE method.

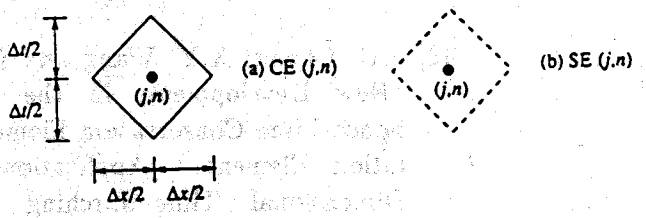

Fig. 3.2 A CE(j,n) and an SE(j,n) of the method of rhombic elements for the mesh point (j,n).

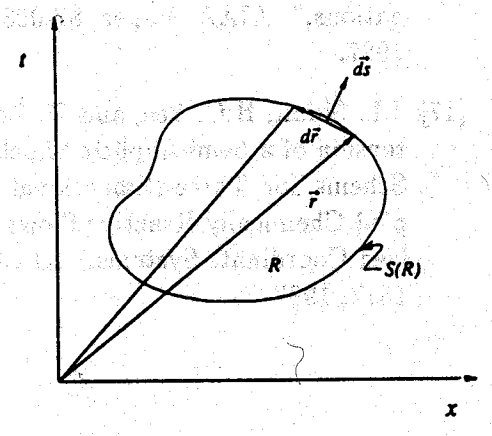

Fig. 2.2 A space-time conservation element with an arbitray space-time domain in one spatial domain.

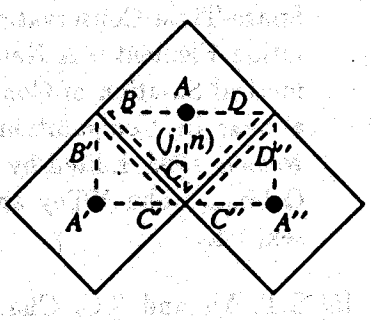

Fig. 3.3 The neighboring CEs (SEs) in the method of rhombic elements.

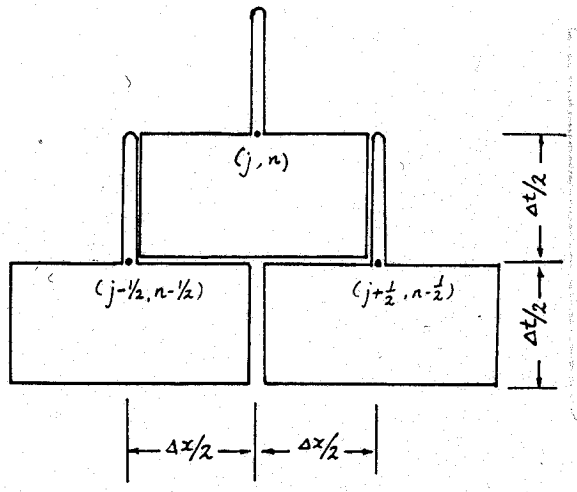

Fig. 3.4 A redistributed SE for stiff source terms in one spatial dimension.

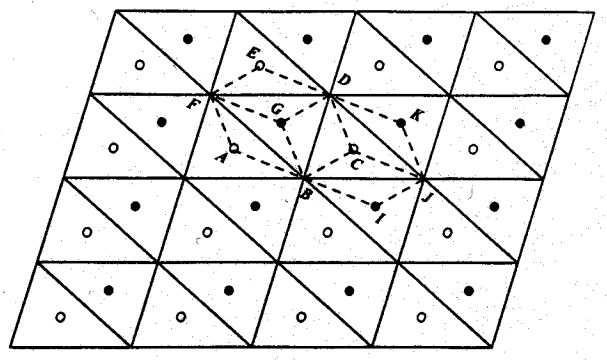

Fig. 3.5 A spatial domain formed by congruent triangles.

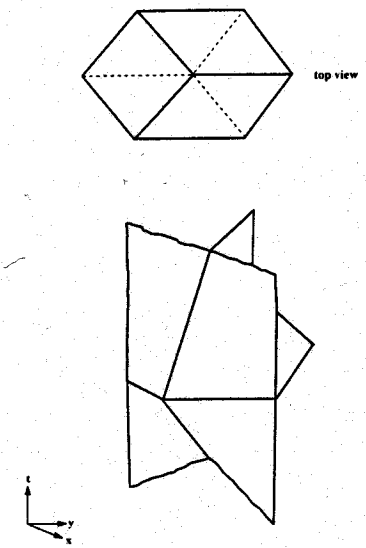

Fig. 3.6 An SE in two spatial dimensions.

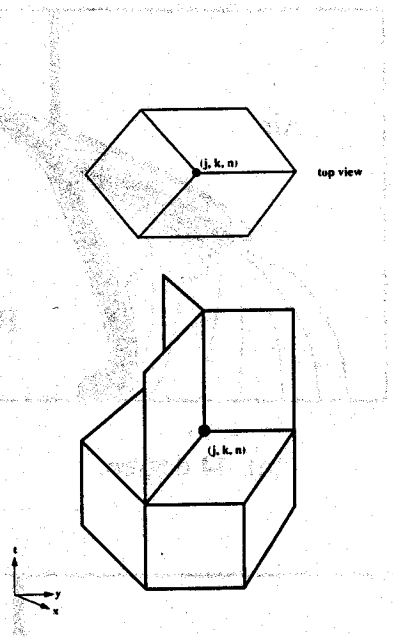

Fig. 3.7 A redistributed SE in two spatial dimensions for stiff source terms.

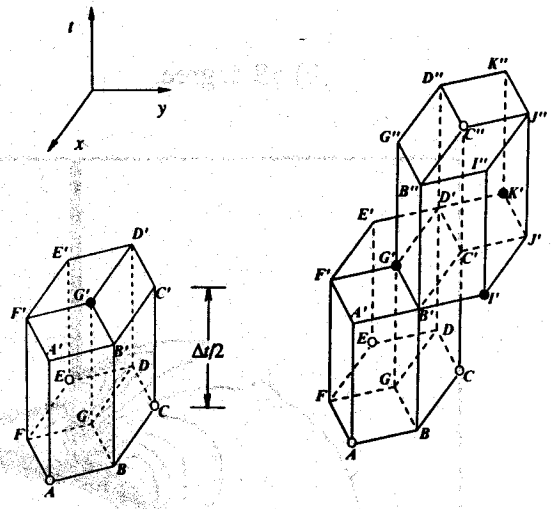

Fig. 3.8 Three CEs associted with G' and the relative positions of CEs of consecutive time steps.

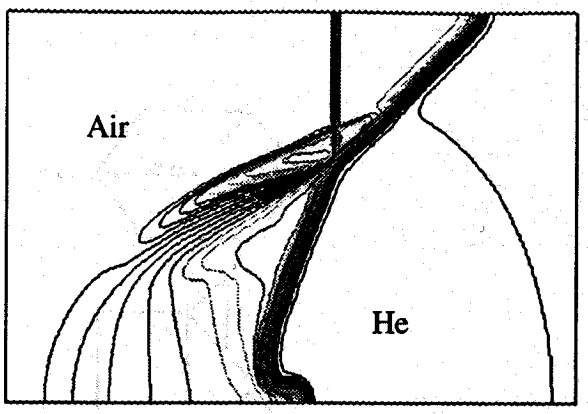

(a) 44 degree.

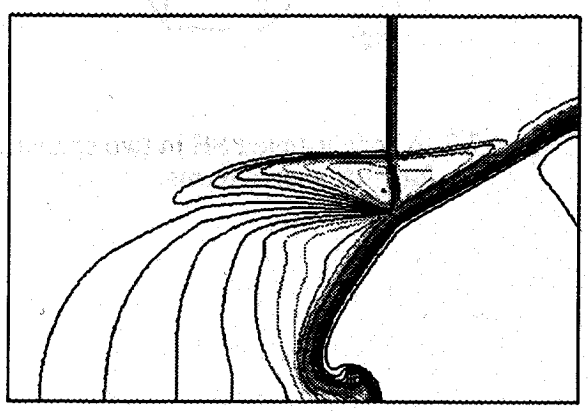

(b) 58 degree.

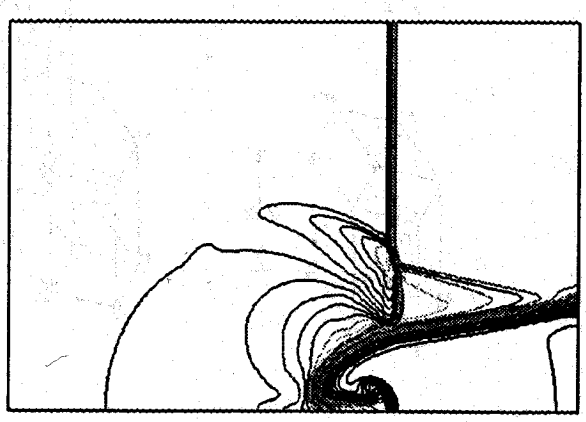

(c) 77 degree.

Fig. 4.1 A planar shock interacts with a straight gaseous interface .

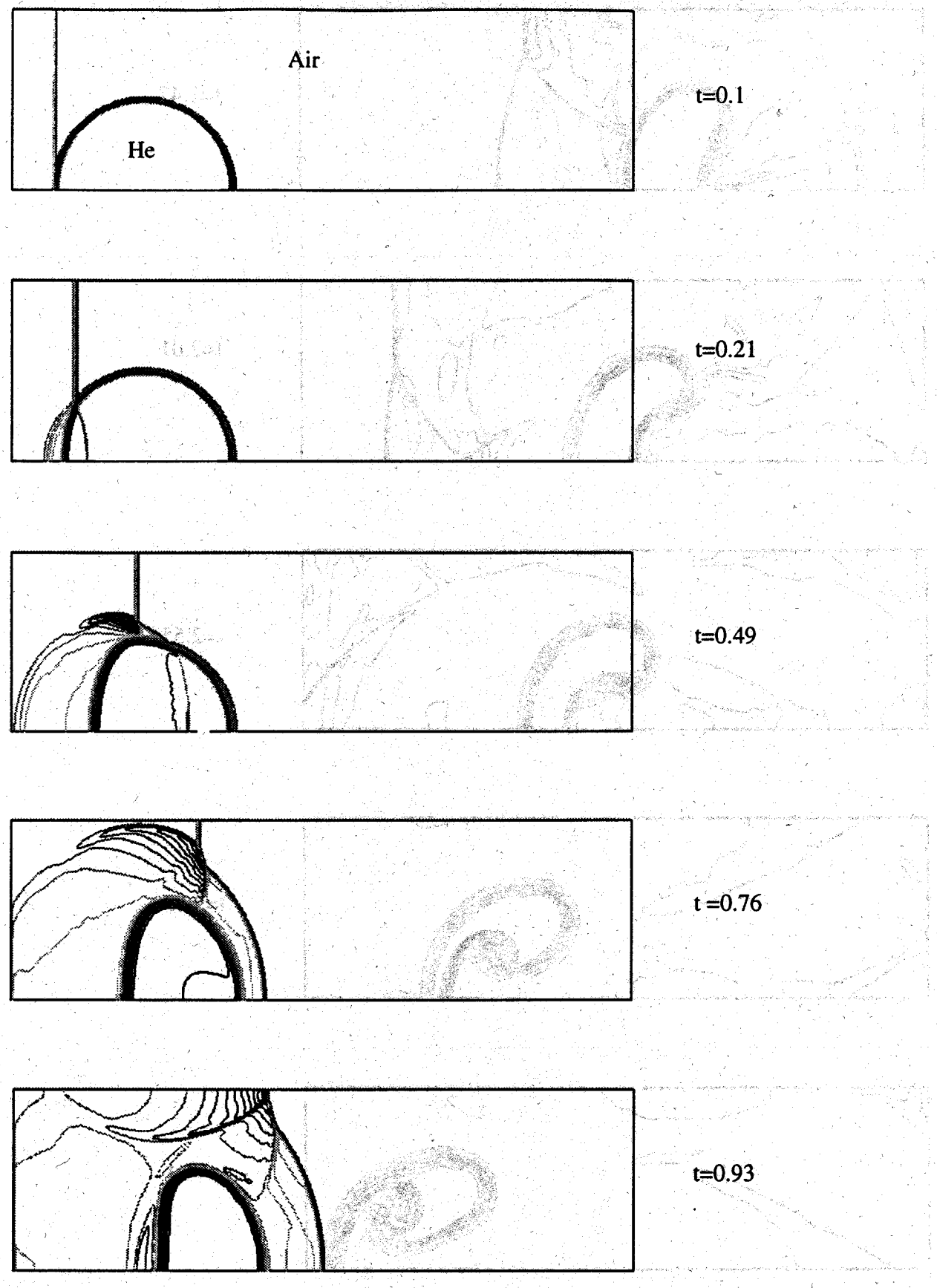

Fig. 4.2 A planar shock interacts with a circular gaseous interface .

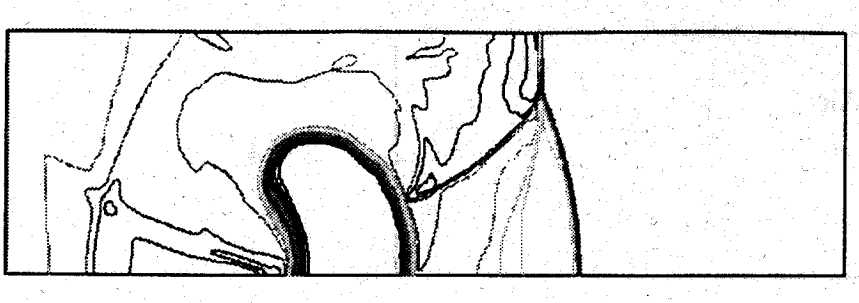

t=1.47

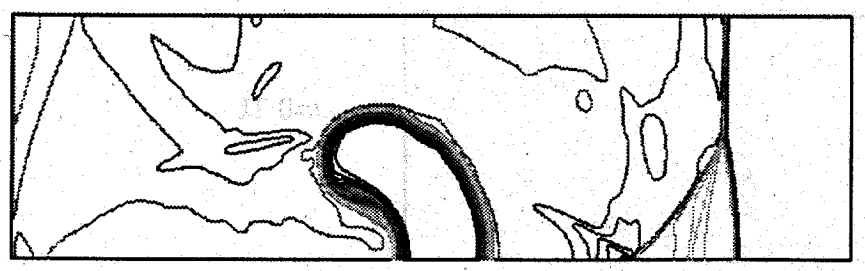

t=2.01

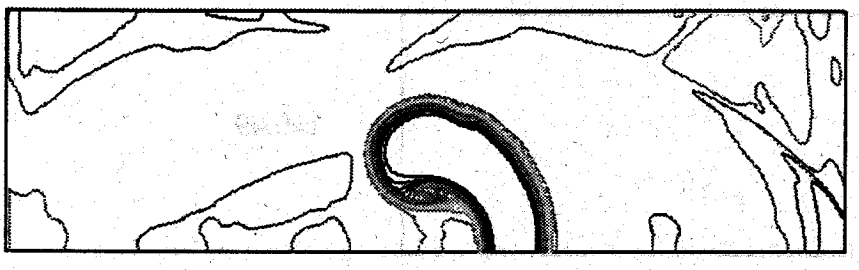

t=2.55

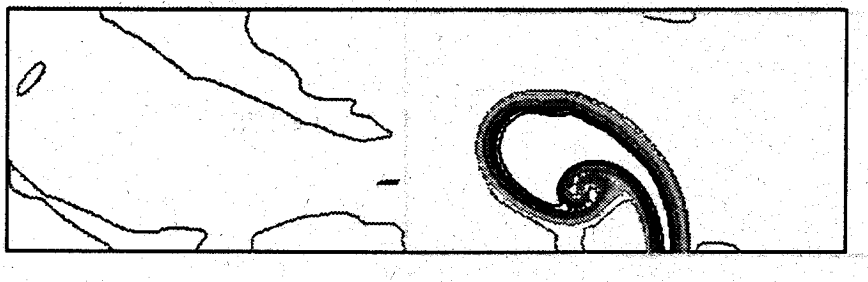

t=3.53

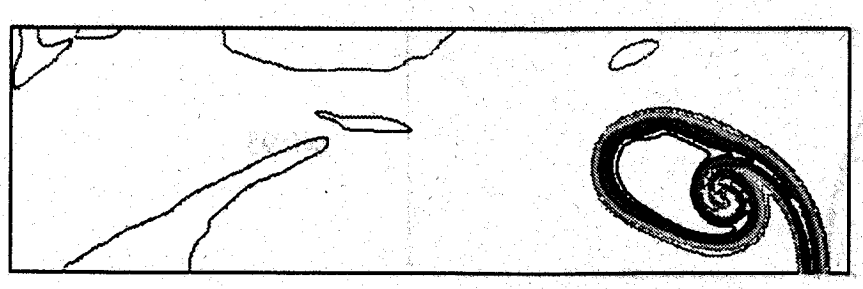

t=4.61

Fig. 4.2

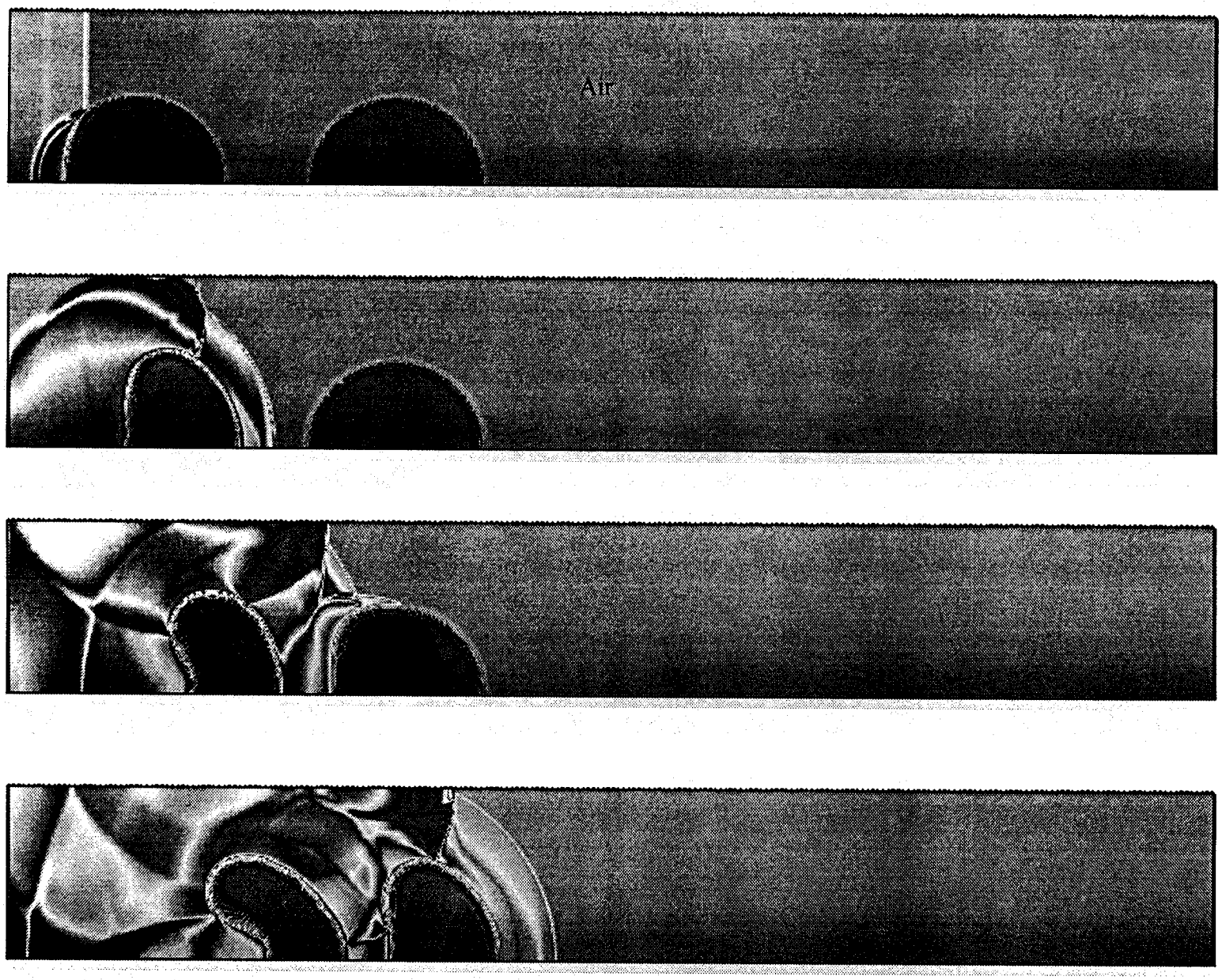

Fig. 4.3 A planar shock interacts with two circular gaseous interfaces.

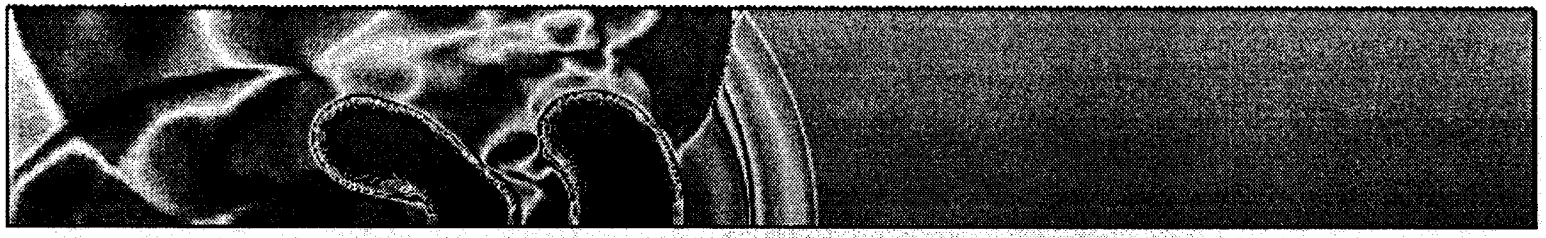

t= 2.28

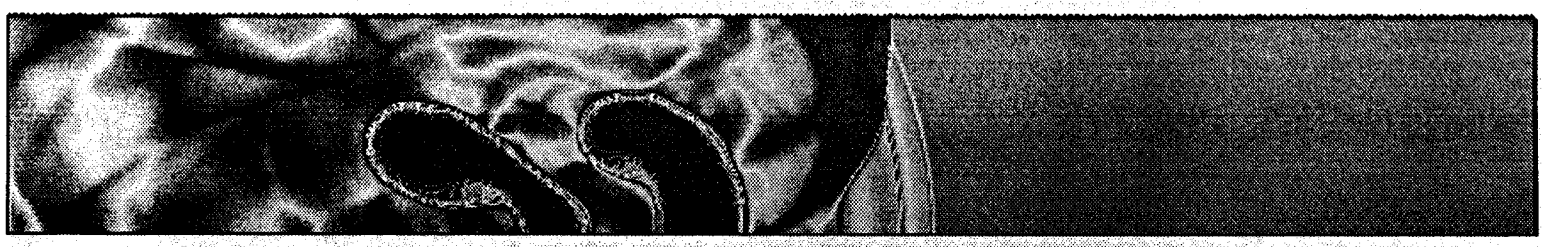

t= 2.78

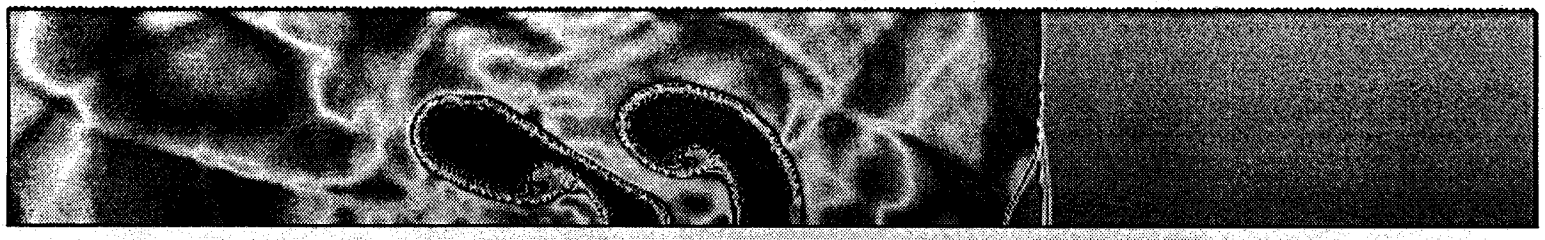

t= 3.28

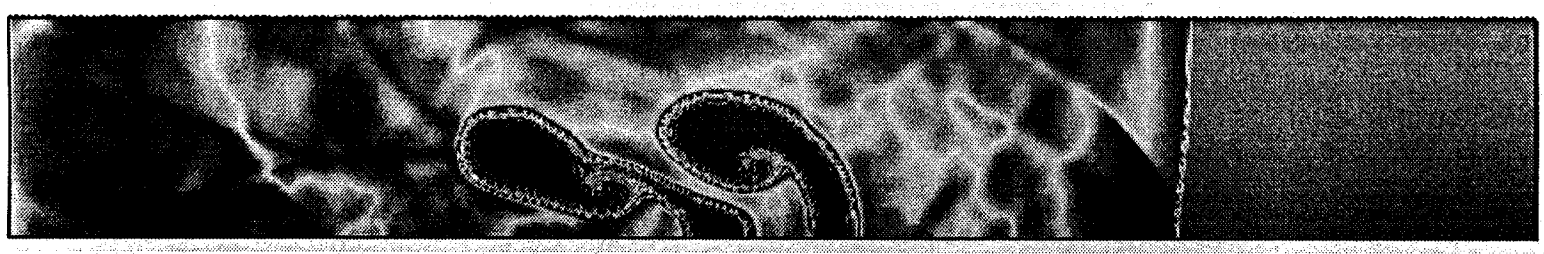

t= 4.03

Fig. 4.3 (b)

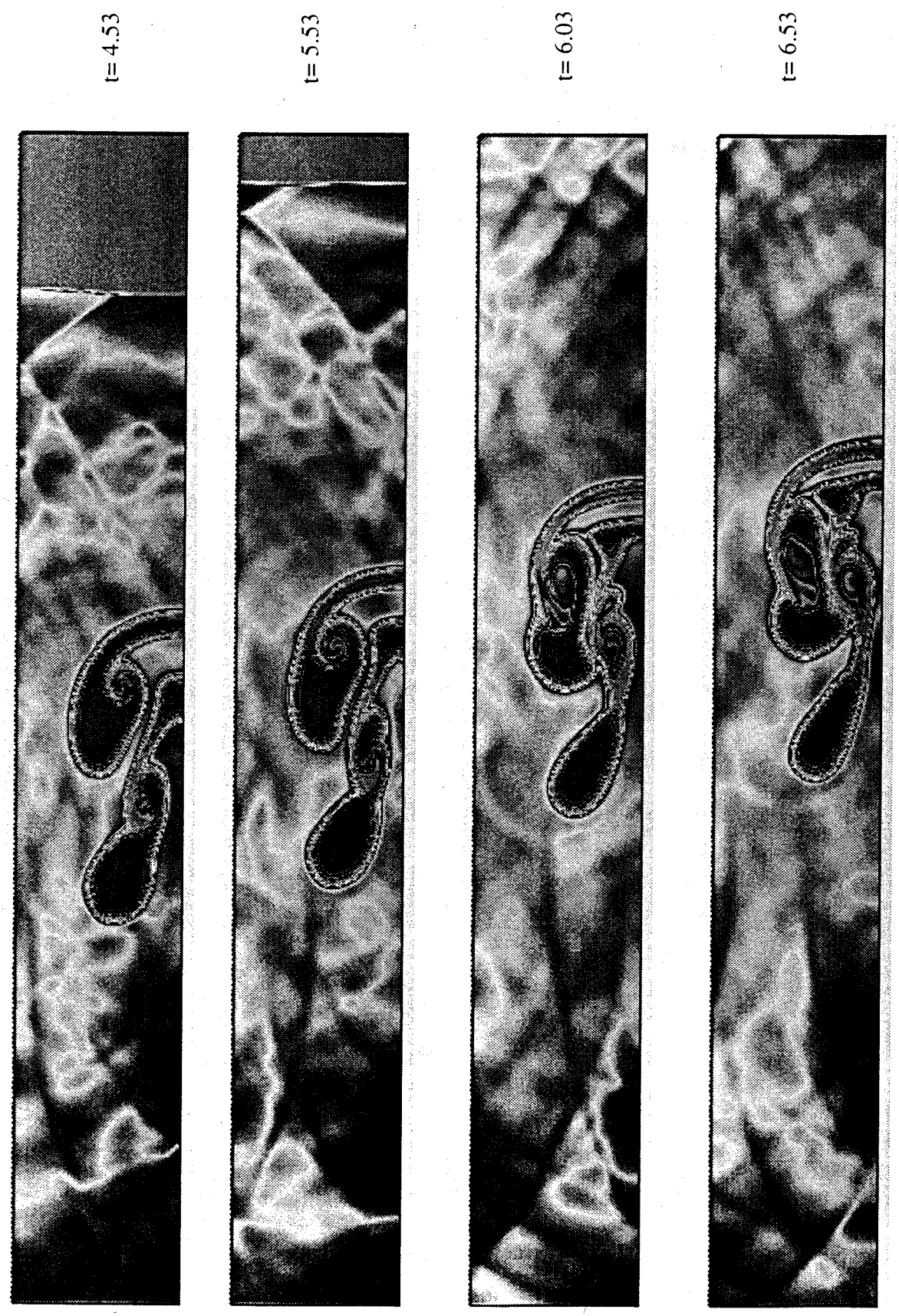

Fig. 4.3(c)

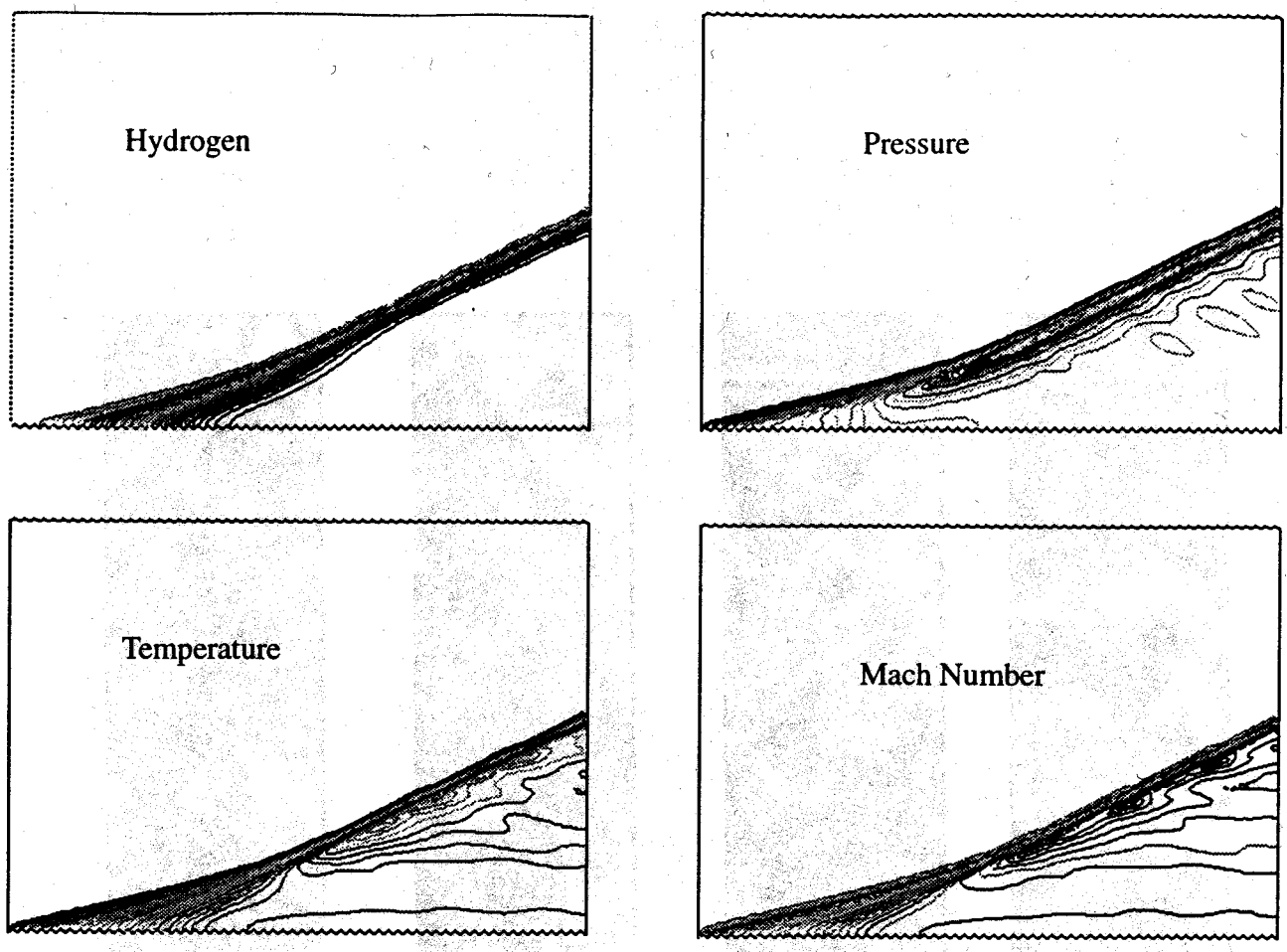

Fig. 4.4 Shock ignited supersonic combustion with free stream Mach number = 4, temperature = 900 K over a 10 degree ramp.

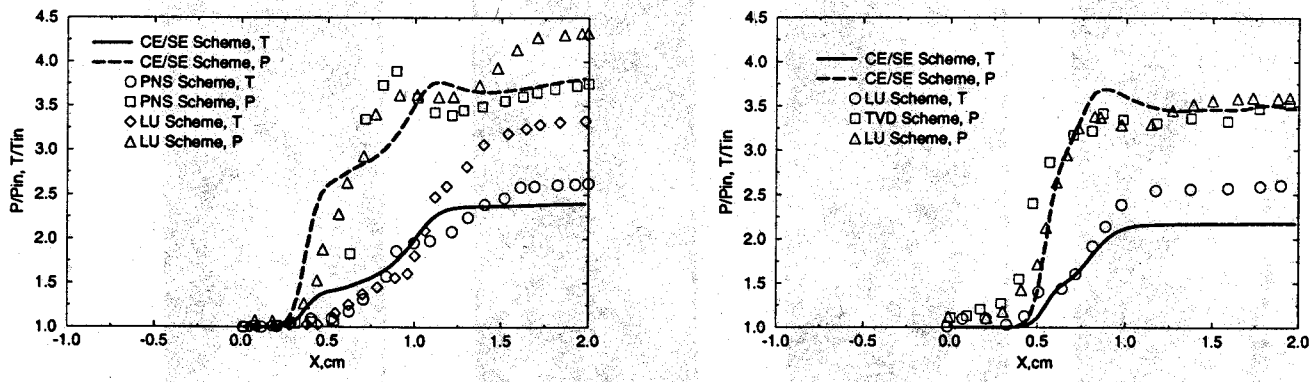

(a) T=900 K. (b) T = 1200 K

Fig. 4.5 The comparison of temperature and pressure between the present calculations and the previous results, including an LU [15], a PNS [16], and a TVD [17] schemes.